Formation of black holes in the pair-instability mass gap: Evolution of a post-collision star

Formation of black holes in the pair-instability mass gap: evolution of a post-collision star

Guglielmo Costa,[1,2,3]★ Alessandro Ballone,[1,2,3] Michela Mapelli,[1,2,3]† Alessandro Bressan,[4]
[1]Physics and Astronomy Department Galileo Galilei, University of Padova, Vicolo dell'Osservatorio 3, I–35122, Padova, Italy
[2]INFN - Padova, Via Marzolo 8, I–35131, Padova, Italy
[3]INAF - Osservatorio Astronomico di Padova, Vicolo dell'Osservatorio 5, I-35122, Padova, Italy
[4]SISSA, via Bonomea 365, I–34136 Trieste, Italy

Accepted XXX. Received YYY; in original form ZZZ

ABSTRACT

The detection of GW190521 by the LIGO–Virgo collaboration has revealed the existence of black holes (BHs) in the pair-instability (PI) mass gap. Here, we investigate the formation of BHs in the PI mass gap via star – star collisions in young stellar clusters. To avoid PI, the stellar-collision product must have a relatively small core and a massive envelope. We generate our initial conditions from the outputs of a hydro-dynamical simulation of the collision between a core helium burning star (~ 58 M$_\odot$) and a main-sequence star (~ 42 M$_\odot$). The hydro-dynamical simulation allows us to take into account the mass lost during the collision (~ 12 M$_\odot$) and to build the chemical composition profile of the post-collision star. We then evolve the collision product with the stellar evolution codes PARSEC and MESA. We find that the post-collision star evolves through all the stellar burning phases until core collapse, avoiding PI. At the onset of core collapse, the post-collision product is a blue super-giant star. We estimate a total mass loss of about 1 M$_\odot$ during the post-collision evolution, due to stellar winds and shocks induced by neutrino emission in a failed supernova. The final BH mass is ≈ 87 M$_\odot$. Therefore, we confirm that the collision scenario is a suitable formation channel to populate the PI mass gap.

Key words: stars:massive – stars:evolution – stars:black holes – black hole physics

1 INTRODUCTION

Stellar collisions can lead to the formation of exotic stars, such as blue stragglers (e.g., Sigurdsson et al. 1994; Sills et al. 1997, 2001; Mapelli et al. 2004, 2006; Glebbeek et al. 2008; Ferraro et al. 2012; Portegies Zwart 2019) and very massive stars (e.g., Portegies Zwart & McMillan 2002; Freitag et al. 2006; Mapelli 2016; Boekholt et al. 2018). In star clusters, stellar collisions are triggered by dynamical interactions, which perturb the orbit of binary stars (e.g., Portegies Zwart et al. 1997, 1999). Multiple collisions among massive stars in a dense star cluster could also lead to the formation of an intermediate-mass black hole (BH) with mass > 100 M$_\odot$ (e.g., Portegies Zwart et al. 2004; Gürkan et al. 2006; Giersz et al. 2015; Mapelli 2016; Di Carlo et al. 2021; Rizzuto et al. 2021; Torniamenti et al. 2022). This process is expected to occur in the early evolution of a star cluster, when the most massive stars sink to the center of the cluster by dynamical friction, undergoing multiple collisions before they die by core collapse (Portegies Zwart et al. 2004). Stellar metallicity is a key ingredient driving the formation of a massive BH via stellar mergers, because stellar winds can dramatically suppress the formation of a very massive star in a metal-rich star cluster (e.g., Glebbeek et al. 2009; Mapelli 2016).

Di Carlo et al. (2019) proposed that stellar collisions in dense star clusters can also trigger the formation of BHs in the pair-instability (PI) mass gap (~ 60–120 M$_\odot$). Massive metal-poor stars are expected to undergo PI at the end of carbon burning, when their hydrostatic equilibrium is compromised by an efficient production of electron–positron pairs in the core. This generally happens if the star develops a He core $\gtrsim 32$ M$_\odot$ and is thought to suppress the formation of BHs with mass $\sim 60-120$ M$_\odot$ (e.g., Heger & Woosley 2002; Belczynski et al. 2016; Woosley 2017, 2019; Spera & Mapelli 2017; Stevenson et al. 2019, but see Farmer et al. 2019, 2020; Mapelli et al. 2020; Marchant & Moriya 2020; Costa et al. 2021; Farrell et al. 2021; Vink et al. 2021 for possible uncertainties on the mass gap). By running direct N-body simulations coupled with population synthesis, Di Carlo et al. (2019) found that the collision between an evolved star, with an already developed He core, and a main sequence (MS) star can result in an exotic star with an oversized envelope with respect to the core. Such a massive star might avoid pair instability and collapse to a BH with mass inside the gap (see also Spera et al. 2019; Kremer et al. 2020; Di Carlo et al. 2020a,b; Renzo et al. 2020b). This new model is one of the most promising scenarios for explaining the formation of GW190521 (Abbott et al. 2020a,b) and other gravitational wave event candidates (Abbott et al. 2021a,b), which are likely associated with BHs in the pair instability mass gap. Vigna-Gómez et al. (2019) showed that stellar mergers are also a promising scenario to produce some hydrogen-rich pulsational pair instability supernovae.

The main limitation of Di Carlo et al. (2019) and similar simulations is that no mass loss is assumed during the collision: the merger product is modeled by assuming that the entire mass of the MS star

★ E-mail: guglielmo.costa@unipd.it
† E-mail:michela.mapelli@unipd.it

wraps around the evolved star. In a companion paper (Ballone et al. 2022) , we take the pre-collision properties of two massive stars from Di Carlo et al. (2020b) and simulate their collision with a hydrodynamical code (StarSmasher; Gaburov et al. 2018). We find that $\sim$ 12% of the total mass is lost during the collision and that the merger product shows evidence of partial mixing between the MS and the evolved star.

Here, we take the outputs of the hydrodynamical simulation performed by Ballone et al. and study the evolution of the merger product with the stellar evolution codes parsec (Bressan et al. 2012; Costa et al. 2019a) and mesa (Paxton et al. 2011, 2013, 2015, 2018, 2019). The hydrodynamical simulation ends when the collision product has reached hydro-static equilibrium but is still far from thermal equilibrium. Here, we relax and evolve the collision product to the end of core oxygen burning (COB) with the parsec code, and to the final collapse with the mesa code.

This article is organized as follows. In Sect. 2, we present the physics adopted in the parsec and mesa stellar evolutionary codes, and describe the post-collision model. We show the results in Sect. 3, and discuss them in Sect. 4. In Sect. 5, we draw our conclusions.

2 METHODS

To compute the stellar model before and after the collision, we used the parsec V2.0 stellar evolutionary code (Bressan et al. 2012; Costa et al. 2019a,b) and the mesa code version 12778 (Paxton et al. 2011, 2013, 2015, 2018, 2019).

2.1 parsec configuration and pre-collision models

For the parsec stellar tracks, we adopt the Caffau et al. (2011) solar composition and compute non-rotating models with an initial metal content $Z = 0.0002$ and a helium content $Y = 0.249$ (from solar calibrations by Bressan et al. 2012). We use the Schwarzschild criterion (Schwarzschild 1958) to define convective unstable borders. We use the mixing length theory framework to compute the diffusion coefficients within unstable regions, with $\alpha_{\rm MLT} = 1.74$. For the overshooting region, we use the penetrative overshooting scheme described in Maeder (1975) and Bressan et al. (1981). We use an overshooting parameter[1] $\lambda_{\rm ov} = 0.4$ (Costa et al. 2019a). We adopted the opacities, neutrinos, equation of state, nuclear reaction network, and stellar winds described in detail in Costa et al. (2021).

Following Di Carlo et al. (2020b), the two components of the binary system are a core helium burning (CHeB) star with an initial mass $M_1 = 57.6$ M$_\odot$, and a MS star with an initial mass of $M_2 = 41.9$ M$_\odot$. In the simulation by Di Carlo et al. (2020b), the two stars merge after 4.3 Myr. Due to the intrinsic differences between the stellar tracks of Di Carlo et al. (2020b) (i.e. mobse evolutionary tracks, Giacobbo et al. 2018) and parsec , we decided to build the pre-collision primary star by matching the evolutionary phase of the two stars rather than the exact age of the collision. Therefore, we computed the evolution of the primary star from zero-age MS (ZAMS) to the CHeB phase, stopping the computation when the star has a central helium content $X_{\rm c}({\rm He}) \sim 0.72$ (in mass fraction). We evolve the secondary star until the central hydrogen is $X_{\rm c}({\rm H}) \sim 0.5$, during the MS phase.

[1] The overshooting parameter $\lambda_{\rm ov}$ is the mean free path in pressure scale height unity that can be traveled by a convective eddy before dissolving, across the convective border.

At these selected stellar stages, the primary star has a helium core of $M_{\rm He} = 27.16$ M$_\odot$, while the secondary star is in the middle of the MS and has a convective core of 23.7 M$_\odot$. It contains 25.8 M$_\odot$ of H and 16 M$_\odot$ of He, distributed between the core and the envelope. Figure 1 shows the chemical profiles of the primary and secondary parsec models.

The two stellar models are used as initial conditions for the SPH simulation by Ballone et al. (2022, briefly described in Section 2.3). In this work, we use such profiles as starting points for the reconstruction of the post-collision star (as described in Section 2.4). For comparison, we also compute two parsec stellar tracks with an initial mass of 57.6 M$_\odot$ (hereafter, p58) and 88 M$_\odot$ (hereafter, p88), respectively. At 4.3 Myr, the p58 star track has already ended the COB phase and is just a few days from the final core collapse (CC).

2.2 mesa models and pre-collision models

For the mesa evolutionary tracks, we adopted the same configuration as Renzo et al. (2020b, hereafter R20)[2]. All mesa models are computed using a metallicity $Z = 0.0002$. Here, we describe the main differences in the adopted physics with respect to the parsec configuration. We refer to R20 for a detailed description of the input physics of the mesa models. The mesa stellar tracks are computed using the Ledoux criterion to define the convective borders (Ledoux 1947), and the diffusion coefficient is calculated by adopting the mixing length theory framework with $\alpha_{\rm MLT} = 2.0$. We use the MLT++ artificial enhancement of the convective flux (Paxton et al. 2015). Overshooting is calculated by adopting the step scheme and following Brott et al. (2011). Thermohaline mixing is included as in Farmer et al. (2016). The pre-collision models are computed with an 8-isotope α chain nuclear network, while for post-collision models a 22-isotope network is adopted.

We built two mesa pre-collision models, taken from two different phases of the primary stellar track (hereafter, m58), that is computed from the zero age main sequence (ZAMS) to the end of CHeB. In the first case, we assume that the primary star collides while in the terminal age main sequence phase, as assumed by R20. The star is a blue super giant (BSG) with a radius of $\approx$ 45 R$_\odot$, and has a well-developed He-core of about 29 M$_\odot$. Panel (e) of Fig. 1 shows the chemical profile of this model.

In the second case, we assume that the primary star is in the CHeB phase with a central helium $X_{\rm c}({\rm He}) \sim 0.74$. At this stage, the primary is a red super giant (RSG) with a radius of about 650 R$_\odot$ and has a He-core of 30.4 M$_\odot$. For computing the latter model, we suppressed the stellar winds since when the star approaches the RSG stage they can remove several solar masses before we reach the desired stopping condition. In the RSG phase, the mass loss could reach about 10^{-4} M$_\odot$yr^{-1}. By suppressing the winds, we can build the primary star in CHeB with 57.6 M$_\odot$. Panel (f) of Fig. 1 shows the chemical profile of this model. We chose this evolutionary stage to make a comparison with the parsec primary star model.

2.3 Hydro-dynamical simulations

As detailed in a companion paper (Ballone et al. 2022), we have run the hydrodynamical simulation of the collision between a CHeB star and a MS star, to infer the properties of their post-collision remnant. Such a simulation has been run with the smoothed particle hydrodynamics (SPH) code StarSmasher (Gaburov et al. 2018),

[2] Publicly available at the following link 10.5281/zenodo.4062492.

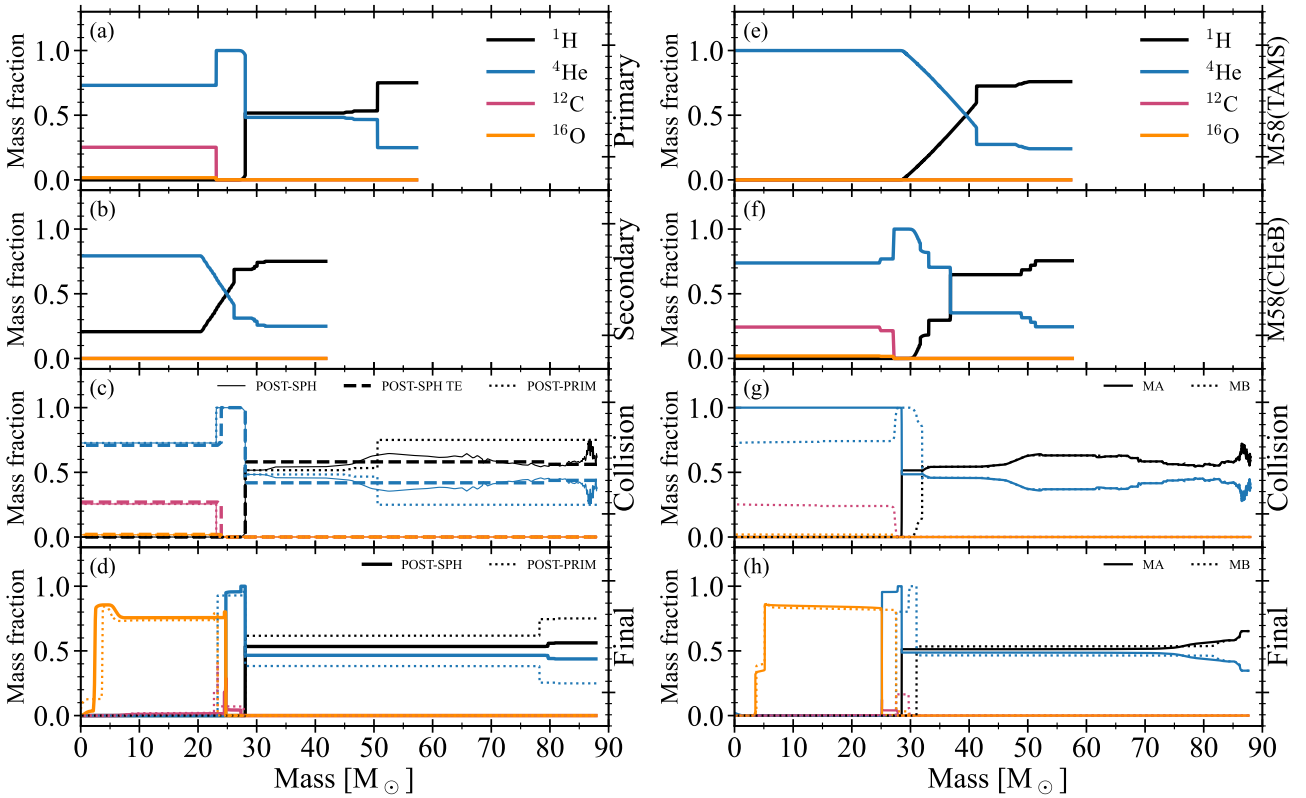

Figure 1. Chemical profiles in mass fraction of hydrogen (black), helium (blue), carbon (pink) and oxygen (orange) of different stellar models. Panels (a) and (b) show the PARSEC primary and secondary profiles before the collision, respectively. In panel (c), the thin solid and dotted lines are the POST-SPH and POST-PRIM models right after the collision, while the thick dashed line is the POST-SPH at thermal equilibrium (POST-SPH TE). Panel (d) shows the profiles of the post-collision PARSEC tracks (POST-PRIM and POST-SPH) at the end of COB. Panels (e) and (f) show the profiles of the MESA track M58, in the terminal age MS and CHeB phases, respectively. These two models are used to build the MESA post-collision tracks MA and MB. Panels (g) and (h) show the profiles of the post-collision MESA tracks (MA and MB) just after the collision and at the onset of the CC, respectively.

Table 1. List of stellar tracks.

Model name	Code	$M_{\rm in}/M_\odot$	Description
Single stellar tracks			
P58	PARSEC	57.6	Star evolved from ZAMS to the end of COB phase.
P88	PARSEC	88	Star evolved from ZAMS to the end of COB phase.
M58	MESA	57.6	Star evolved from ZAMS to the end of CHeB phase.
Post-collision stellar tracks			
POST-PRIM	PARSEC	88	The evolution starts as a RSG in CHeB phase with a primordial envelope composition.
POST-SPH	PARSEC	88	The evolution starts as a RSG in CHeB phase, with the SPH simulation envelope composition.
MA	MESA	88	The evolution starts as a BSG star in the terminal age MS phase. The same envelope composition as in the SPH simulation.
MB	MESA	88	The evolution starts as a BSG star in the CHeB phase. Same envelope composition as in the SPH simulation.
MIX	MESA	99	Track with a complete mixed envelope from R20.
PRIMORDIAL	MESA	99	Track with a primordial envelope composition from R20.

The models MIX and PRIMORDIAL are the mix and primordial models of R20, that we re-ran using their configuration.

which is particularly well-suited for simulations of stellar mergers. We generated the initial conditions for the colliding stars by importing the one-dimensional profiles obtained with PARSEC (see Section 2.1) and then re-mapped them into three-dimensional distributions of SPH particles. To test the most extreme case in terms of mass lost in the collision, we put the stars on a radial orbit, with a velocity at infinity equal to 10 km s^{-1}, corresponding to the typical velocity dispersion of young massive star clusters.

We evolved the stellar remnant with StarSmasher until it reached the hydrodynamical equilibrium, and found that about 12% of the total mass of the system is ejected during the collision, so that the post-coalescence star has a final mass equal to 87.9 M$_\odot$. We also

found that in the encounter the MS star sinks down to the close vicinity of the He-burning core of the primary star, while the material lost mostly belongs to the outer H-rich envelope of the CHeB star. As a result, the chemical abundances re-arrange according to the profile shown in Fig. 1. More details on the setup and results of this hydrodynamical simulation can be found in Ballone et al. (2022). From this hydro-dynamical simulation we take the information about the mass loss and the final chemical profile[3]. We use this information to build a new stellar model by means of an accretion process, as detailed in the following section (see also R20).

2.4 Constructing the post-collision model

2.4.1 PARSEC

To construct the post-collision star with PARSEC, we accrete mass onto the primary star until its total mass becomes $M_{\rm coll}$ = 88 $M_\odot$. During accretion, we stop the chemical evolution and take into account the heat injected by the accreting material, as described by Kunitomo et al. (2017), which leads the star to inflate and become a RSG. Such expansion is expected from a head-on collision process (Sills et al. 1997; Glebbeek et al. 2008, 2013; Ballone et al. 2022). More details on the accretion process are provided in the Appendix A. After mass accretion, we create two post-collision models. In the first model (hereafter POST-PRIM) we maintain the pristine chemical composition of the envelope, while in the second model (POST-SPH) we change the chemical composition of the envelope to match the SPH simulation by Ballone et al. (2022). Panel (c) of Fig. 1 shows the chemical profiles of the two models, POST-PRIM and POST-SPH. Both post-collision models have a helium core of $\sim$ 28 $M_\odot$, and an envelope of about 60 $M_\odot$, by construction. The model POST-PRIM has a total He content of 41.5 $M_\odot$, while the model POST-SPH has 46.7 $M_\odot$. Then, we restart the chemical evolution and follow the evolution of the two stars until the end of the COB phase.

2.4.2 MESA

To construct the post-collision star with MESA, we use the methodology described in R20. In the first step, the mass is accreted onto the primary model until the total mass reaches $M_{\rm coll}$= 88 $M_\odot$. Then, we changed the chemical profile of the envelope to reproduce the SPH simulation. During such building steps, the chemical evolution is stopped. In agreement with R20, but in contrast with the method we used for the PARSEC models, we do not include extra heating injection during the accretion. This methodology leads the models of the post-collision products to be luminous BSG.

With the above methodology, we compute two MESA post-collision tracks. The first (hereafter MA) is built assuming that the primary star is in the terminal age MS phase, therefore we start the accretion from the primary model M58(TAMS). The MA track right after the collision has a He-core of about 29 $M_\odot$, and a total helium content of about 55 $M_\odot$.

The second track (MB) is built assuming that the primary is in the CHeB phase, then we start the accretion from the M58(CHeB) model. We accrete mass until the total mass reaches $M_{\rm coll}$, and then change the chemical composition of the envelope. This post-collision model has a He-core of about 30 $M_\odot$, a total helium content of about 47 $M_\odot$, and a total carbon and oxygen content of about 7 $M_\odot$. Panel (g) of Fig. 1 shows the chemical profiles of the two reconstructed models with MESA right after the collision. We follow the evolution of the two stars until the onset of CC. The *inlists* of the MESA models and outputs are available at 10.5281/zenodo.6418976. Table 1 lists all computed tracks and their main properties.

[3] We do not use the full profiles derived from the hydro-dynamical simulation, because the resolution of the He core is not suitable for entropy relaxation with a stellar-evolution code (Ballone et al. 2022).

3 RESULTS

3.1 Post-collision evolution

Figure 2 shows the evolution of the post-collision stellar tracks in the Hertzsprung-Russell (HR) diagram. The left-hand panel shows the comparison of POST-PRIM and POST-SPH with the "standard" stellar tracks P58 and P88. Both post-collision tracks start their evolution as RSGs. During the RSG phase, they undergo a relatively high mass loss (2×10^{-5} $M_\odot yr^{-1}$) by stellar winds. They rapidly evolve toward the blue part of the HR diagram, reaching thermal equilibrium in $\sim 8 \times 10^3$ yr and $\sim 5.5 \times 10^3$ yr for POST-PRIM and POST-SPH, respectively. This time scale is several times the Kelvin-Helmholtz time-scale of the models at the beginning of their evolution, that is, about 100 yr. When they reach thermal equilibrium, they have lost less than 0.05 $M_\odot$, and restart burning helium in a stable way. Panel (c) of Fig. 1 shows the profile of the track POST-SPH in TE. During thermal relaxation, the star develops large convective regions which rapidly homogenize the envelope. The small inversion of molecular weight in the post-collision model is canceled by convection. Therefore, mixing processes due to molecular weight inversions (i.e., thermohaline mixing) do not take place during the evolution. In this phase, both models still have a central helium fraction of about X_c(He) $\sim$ 0.7. The higher luminosity of the POST-SPH track compared to the POST-PRIM track depends mainly on the different helium content in the stellar envelope and surface. Generally, stars with a stellar surface enriched with He are more luminous, due to the higher mean molecular weight (Kippenhahn et al. 2012).

After thermal relaxation, the stellar tracks POST-SPH and POST-PRIM are BSGs, with a radius of about 25 $R_\odot$ and 31 $R_\odot$, respectively. The mass loss by stellar winds is quenched ($\sim 3 \times 10^{-7}$ $M_\odot$ yr^{-1}). During the CHeB phase, the stars move to the red part of the HR diagram. The CHeB phase of the two stars lasts for $\sim 2.4 \times 10^5$ years for POST-PRIM and $\sim 2.2 \times 10^5$ years for POST-SPH. After CHeB, both stars evolve until the end of COB in $\sim 4 \times 10^3$ years and end their life as BSGs. These stars retain most of their envelope during evolution due to inefficient line-driven winds (Vink et al. 2021). In contrast, the standard tracks P58 and P88 end their life as RSGs. The different final stellar configuration may have an impact on the final mass of the BH, since RSG stars may shed their envelope during core collapse, because of neutrino loss (Fernández et al. 2018).

The right-hand panel of Fig. 2 compares the post-collision MESA tracks and the POST-SPH track. In the same Figure, we added the MIX and PRIMORDIAL post-collision tracks from R20 for comparison. By construction, the MESA tracks begin their evolution as BSGs. After a brief expansion phase, they start the CHeB phase and move to lower effective temperatures. All MESA models end their life as BSGs. This Figure shows that the post-collision stellar tracks with the total mass equal to $M_{\rm coll}$ and the reconstructed stellar envelope from the SPH simulation have a very similar evolutionary path, even if they have been built with a different methodology and simulated with a different stellar evolution code. The MESA tracks tend to end their life with larger stellar radii than the PARSEC tracks. Table 2 shows the properties of the stellar tracks at the end of COB and at the onset of CC for the MESA models.

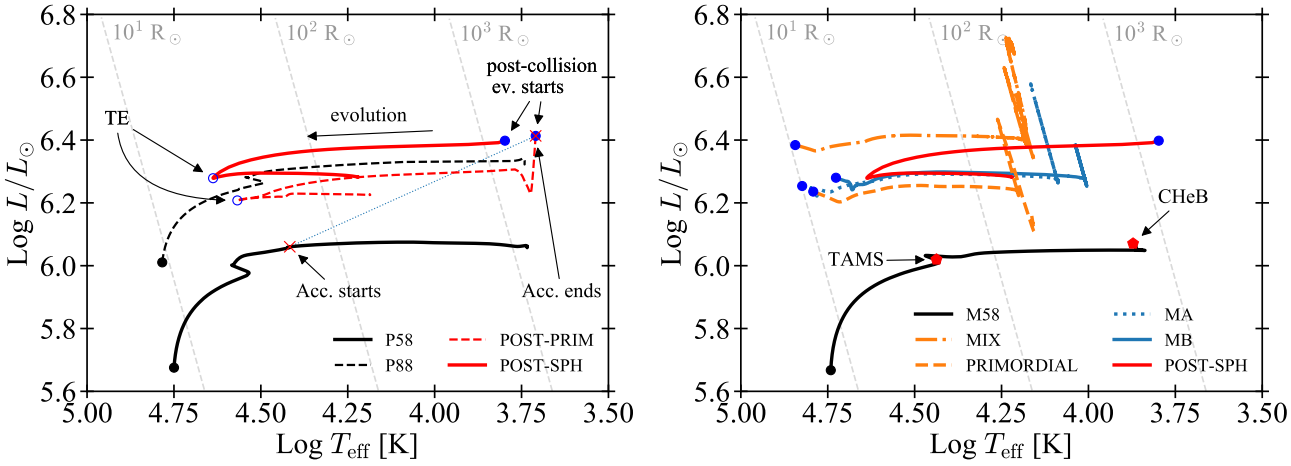

Figure 2. HR diagrams of the post-collision models. The left-hand panel shows the PARSEC tracks. The black points indicate the ZAMS of the standard (single-star) tracks. The black solid line indicates the evolution of the primary star (P58). The red crosses mark the starting and ending points of the accretion process, which are connected by the thin blue dotted line. The blue points indicate the starting point of the post-collision evolution tracks. The red dashed line shows the evolution of the post-collision track with pristine gas composition (POST-PRIM). The red solid line shows the evolution of the POST-SPH track, in which we changed the chemical composition according to the SPH simulation. The blue empty circles mark the point in which the post-collision tracks reach thermal equilibrium (TE). The black dashed line shows the evolution of the P88 star track. The right-hand panel shows the MESA tracks. The black point and the solid line indicate the ZAMS and the evolution of the primary track M58. The blue points indicate the starting point of the post-collision evolution tracks. The dashed and dot-dashed orange lines are the MIX and PRIMORDIAL models from R20, respectively (the MIX model assumes complete chemical mixing, while the PRIMORDIAL model assumes no mixing). The dotted and solid blue lines are the models MA and MB, respectively. The solid red line is the PARSEC track POST-SPH, for comparison. The two red pentagons mark the two evolutionary stages we use to construct the MESA post-collision models MA and MB, terminal age MS (TAMS) and CHeB.

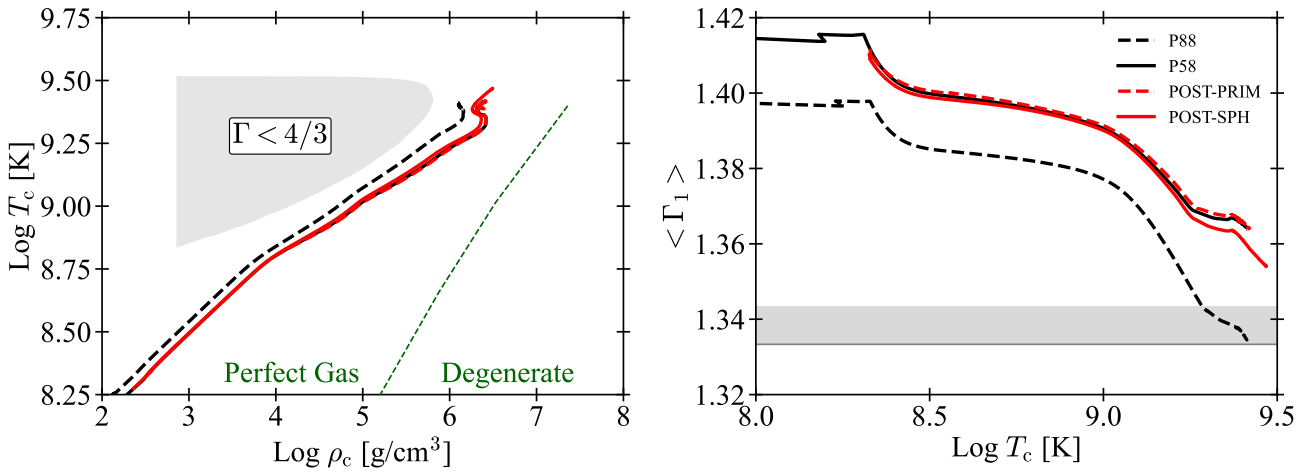

Figure 3. The left-hand panel shows the evolution of the central temperature versus central density of the post-collision tracks. The right-hand panel shows the evolution of $\langle\Gamma_1\rangle$ as a function of the central temperature. In both panels, black dashed line: track P88; black solid line: P58; red dashed line: POST-PRIM; red solid line: POST-SPH. The grey area in the left-hand panel indicates the instability region with $\Gamma_1 < 4/3$. In the right-hand panel, the thin dark gray horizontal line corresponds to $\langle\Gamma_1\rangle = 4/3$. The above light-gray area indicates values of $\langle\Gamma_1\rangle$ between 4/3 and 4/3 + 0.01, i.e. the range in which the whole star becomes dynamically unstable (Farmer et al. 2019; Costa et al. 2021). The post-collision tracks (POST-SPH and POST-PRIM) almost overlap with the track P58 (with mass 57.6 M$_\odot$) in both diagrams.

Figure 3 shows the evolution of the central temperature (T_c), density (ρ_c), and pressure-weighted average adiabatic index ($\langle\Gamma_1\rangle$, Farmer et al. 2020; Renzo et al. 2020a; Costa et al. 2021) of the PARSEC tracks. The tracks POST-PRIM and POST-SPH almost overlap with track P58 in the figure, because they have a very similar He core. These models avoid PI (i.e., $\langle\Gamma_1\rangle > 4/3$ during the whole evolution) and will eventually undergo CC. The final BH mass depends on the pre-supernova total mass and on the fate of the envelope during collapse (as discussed in Sect. 4).

The 'standard' PARSEC stellar track P88, builds up a bigger He core during the CHeB phase ($M_{\rm He} \approx 46$ M$_\odot$) with respect to the exotic post-collision stars, and becomes unstable to PI during the COB phase (in an off-center region, Woosley 2019; Farmer et al. 2020; Renzo et al. 2020a; Costa et al. 2021).

Figure 4 shows the evolution of T_c, ρ_c, and $\langle\Gamma_1\rangle$ for the MESA

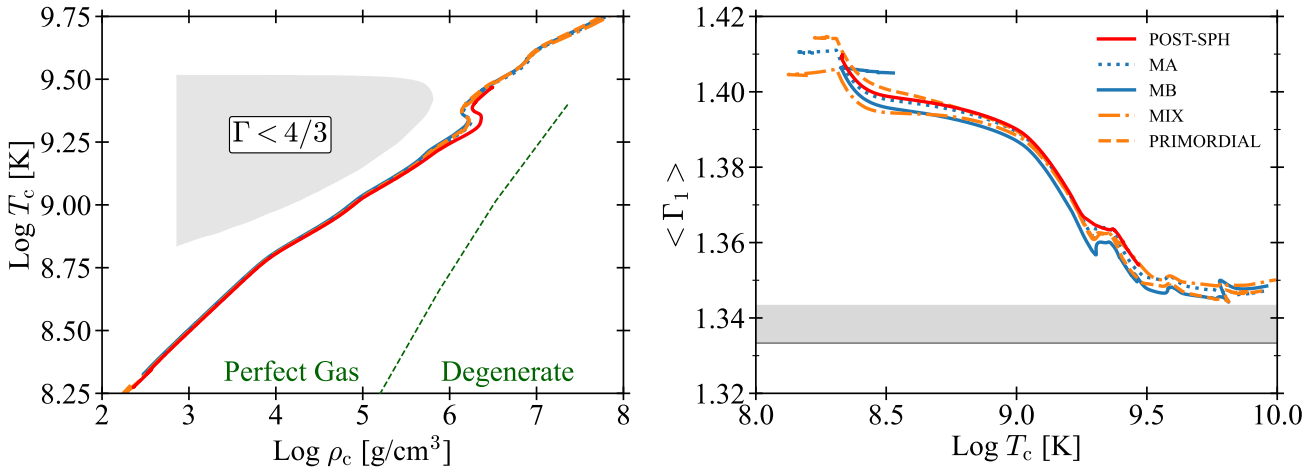

Figure 4. Comparison between PARSEC and MESA tracks. Left-hand panel: central temperature versus central density; right-hand panel: $\langle\Gamma_1\rangle$ versus the central temperature. In both panels, the red solid line is the PARSEC POST-SPH track, while the blue dotted and dashed lines are the MESA tracks MA and MB, respectively. The orange dot-dashed and dashed lines are the R20 post-collision tracks MIX and PRIMORDIAL, respectively.

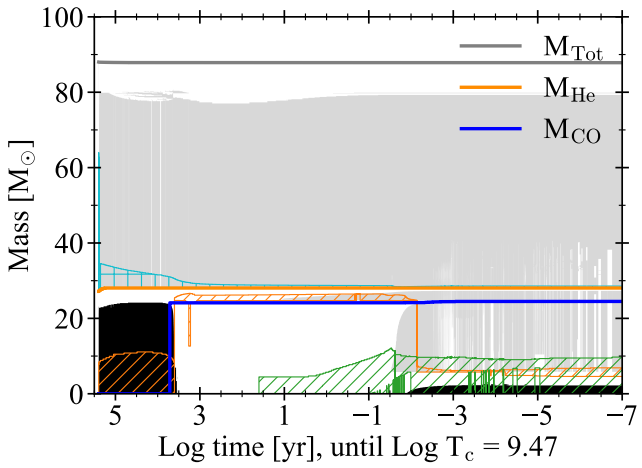

Figure 5. Kippenhahn diagram of the post-collision stellar track POST-SPH. The black area is the convective core, the grey areas indicate the convective envelope and intermediate convective regions. Continuous gray, yellow, and blue lines show the total stellar mass, He core mass and CO core mass, respectively. The cyan, yellow, and green hatched areas indicate the hydrogen, helium and carbon burning regions, respectively. We plot zones that contribute at least for the 1% to the H, He and C luminosity at a given time-step.

tracks. The evolutionary paths of these stellar tracks are very similar, as they all evolve from the CHeB phase to the final CC avoiding PI. This Figure shows that the POST-SPH track evolves in a similar way to the MESA tracks (MA and MB).

Figure 5 shows the evolution of the internal structure of the track POST-SPH. During the CHeB phase, the star has a convective core that extends up to about 28 $M_\odot$, and a large intermediate convective region in the envelope fueled by the hydrogen-burning shell. After CHeB, core convection is quenched, and the core contracts while the envelope expands. In this phase, the star has a double burning shell in which helium burns above the CO core, while hydrogen burns above the He core. About 70 yr before the final collapse, the star ignites carbon in the core. When central carbon is depleted, the carbon burning shell moves outward and triggers an internal convective zone. The energy provided by the carbon-burning shell sustains the external layers of the star and prevents PI (Woosley 2019; Farmer et al. 2020; Costa et al. 2021). In this phase, neon photo-disintegration occurs, and when the central temperature reaches ~ 2 GK, oxygen is ignited (~ 6 days before the final collapse). Oxygen burns in a small convective core of about 2.2 $M_\odot$. At the end of the computation (that is, when the central oxygen is depleted), the central core is composed of 2.8% of ^{23}Na, 38% of ^{28}Si, 36% of ^{32}S, 10% of ^{36} Ar, and 13% of ^{40}Ca. After this stage, in a few hours, the star will burn silicon and undergo the final CC.

3.2 Core and envelope compactness

We compute the core compactness, $\xi_{2.5}$, of the last model of our simulations following O'Connor & Ott (2011) and references therein:

$$\xi_{2.5} = \frac{2.5}{r(M = 2.5\ M_\odot)/10^3 \mathrm{km}}, \quad (1)$$

where $r(M = 2.5\ M_\odot)$ is the radius that encloses 2.5 $M_\odot$. We also computed the envelope compactness, $\xi_{\rm env}$, which is a proxy for the surface gravity of the star:

$$\xi_{\rm env} = \frac{M_*}{R_*}, \quad (2)$$

where M_* and R_* are the total mass and radius of the star. We compute the compactness of the core and envelope at the end of the COB phase (which corresponds to the end of the simulation for PARSEC models), and at the onset of CC. The results are shown in the upper and lower panels of Table 2, respectively.

Fernández et al. (2018) have shown that mass ejection can occur even in a failed supernova, because of the instantaneous loss of neutrinos triggering a shock. Extending the previous work of Lovegrove & Woosley (2013) and Lovegrove et al. (2017), Fernández et al. (2018) found that mass ejection can occur in all types of BH progenitors. The energy ejected from the explosion is a decreasing function of $\xi_{2.5}$, while the ejected mass is a decreasing function of $\xi_{\rm env}$.

Figure 6 shows the binding energy of the external parts of the envelope at the end of the COB phase for PARSEC tracks, and at the

Table 2. Properties of the models at the end of COB, and at the onset of CC.

End of core oxygen burning											
Model	$M_*/M_\odot$	$R_*/R_\odot$	Log $L/L_\odot$	Log $T_{\rm eff}$/K	Log g/(cm s^{-2})	$M_{\rm He}/M_\odot$	$M_{\rm CO}/M_\odot$	$\xi_{2.5}$	$\xi_{\rm env}$	$M_{\rm ej}/M_\odot$	$M_{\rm BH}/M_\odot$
POST-PRIM	87.9	183.7	6.227	4.187	1.854	28.1	23.3	0.250	0.479	0.04 - 0.28	87.3
POST-SPH	87.8	167.2	6.284	4.221	1.935	28.1	24.5	0.279	0.525	0.03 - 0.26	87.3
MIX	98.5	268.1	6.687	4.219	1.575	29.2	25.4	0.293	0.367	-	-
PRIMORDIAL	98.9	187.1	6.138	4.160	1.889	28.9	25.8	0.273	0.528	-	-
MA	87.6	301.5	6.529	4.154	1.422	28.5	25.1	0.277	0.291	-	-
MB	87.7	436.7	6.258	4.006	1.100	31.0	27.5	0.281	0.201	-	-
Onset of core collapse											
Model	$M_*/M_\odot$	$R_*/R_\odot$	Log $L/L_\odot$	Log $T_{\rm eff}$/K	Log g/(cm s^{-2})	$M_{\rm He}/M_\odot$	$M_{\rm CO}/M_\odot$	$\xi_{2.5}$	$\xi_{\rm env}$	$M_{\rm ej}/M_\odot$	$M_{\rm BH}/M_\odot$
MIX	98.5	271.0	6.701	4.220	1.562	29.2	25.6	0.510	0.362	0.03 - 0.27	97
PRIMORDIAL	98.9	188.9	6.158	4.163	1.880	28.9	25.9	0.561	0.523	0.03 - 0.22	97.3
MA	87.6	302.9	6.575	4.165	1.418	28.5	25.1	0.591	0.289	0.04 - 0.36	87
MB	87.7	436.7	6.384	4.037	1.101	31.0	27.5	0.541	0.201	0.06 - 0.43	87

From left to right: track name, stellar mass, radius, luminosity, effective temperature, surface gravity, He core mass, CO core mass, core compactness, envelope compactness, estimated ejected mass in a failed supernova, and expected BH mass. The upper part of the Table shows the values of these quantities at the end of COB, while the lower part indicates the values at the onset of CC. To compute the final mass of the R20 models (MIX and PRIMORDIAL) we take into account the luminous blue variable like outbursts assuming $M_{\rm LBV} = 1\ M_\odot$.

onset of the CC for MESA tracks. All our models die as BSG stars, with envelope compactness between $\xi_{\rm env} = 0.2$ and 0.5 (as shown in Table 2). To give an estimate of the mass ejected by neutrino loss, we assume two extreme cases of ejected energy during the CC, from the results of Fernández et al. (2018). Assuming an instantaneous loss of gravitational mass $\delta M_{\rm G} \sim 0.3\ M_\odot$, Fernández et al. (2018) found an ejected energy between 10^{47} and 10^{48} erg for BSGs. The corresponding ejected mass ($M_{\rm ej}$) in the two cases goes from 0.03 $M_\odot$ to 0.43 $M_\odot$ for the most and least compact of our models, respectively (Table 2).

In the final mass estimations, we did not include possible mass loss during CC due to a shock revival that propagates outward after core bounce (Powell et al. 2021; Rahman et al. 2022, and references therein). In the case of pulsational-pair instability progenitors of BHs, Rahman et al. (2022) found that the shock (or sonic pulse) propagating up to the stellar surface may lead to an upper limit of the unbound mass that goes from 0.07 $M_\odot$ to 3.5 $M_\odot$, depending on the progenitor structure. We cannot straightforwardly apply such mass loss to our models, because of the different progenitor physical configuration. In the case of Rahman et al. (2022), the BH progenitor is a stripped star which suffered several episodes strong of mass loss due to the pulsations induced by pair creation.

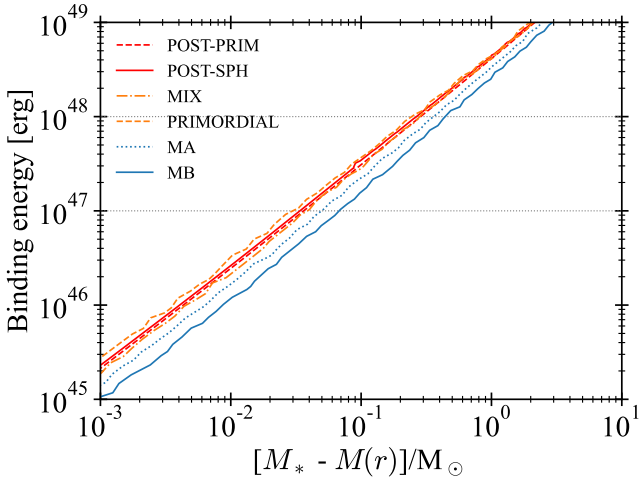

Figure 6. Binding energy of the external part of the stellar envelope, from the exterior to the inner structure of our models, at the end of the evolution. The horizontal dotted gray lines show the minimum and maximum values of energy ejected ($E_{\rm ej}$) in a failed supernova for BSG stars, as found by Fernández et al. (2018)

4 DISCUSSION: THE FINAL BH MASS

We integrated the evolution of an exotic star with a small core and a massive envelope) formed by stellar collision. Such type of BH progenitors may also form via single stellar evolution depending on the stellar physics adopted. The boundaries of the PI mass gap are very sensitive to stellar convection treatment, nuclear reaction rates, and stellar winds (Farmer et al. 2020; Costa et al. 2021; Vink et al. 2021). Here, we investigate in detail the collision scenario, using a standard configuration for the stellar evolution.

Our stellar models come from the results of a hydrodynamical simulation (Ballone et al. 2022), which shows that the mass lost during the collision is not negligible, corresponding approximately to 12% of the total mass of the system. All our models avoid PI and evolve until the final CC (Fig. 4). This happens because the collision leaves the core of the primary star nearly untouched.

We have calculated the core and envelope compactness ($\xi_{2.5}$ and $\xi_{\rm env}$) at the end of the simulations, to have a rough estimate of the mass lost during the final collapse, because of shocks induced by neutrino emission (Fernández et al. 2018). We find that $\xi_{\rm env}$ does not change after the COB phase. This happens because after COB the evolution of the core is very fast and almost detached from the evolution of the envelope. Therefore, we can estimate the mass ejected during the failed supernova ($M_{\rm ej}$) also from models that do

not evolve until the onset of CC. In contrast, the core compactness changes significantly during the last phases. Thus, we cannot estimate the energy ejected during collapse from the models computed up to the end of COB (Chieffi et al. 2021).

All post-collision stellar tracks cross the S Doradus instability strip during the CHeB or core carbon burning phases and evolve beyond the Humphrey-Davidson limit. In such regions, a star may suffer from opacity-driven outburst episodes, typical of luminous blue variable stars. R20 found that stellar merger products may live for hundreds of years in proximity to the Eddington luminosity limit, and estimated that the total mass lost from the outbursts ($M_{\rm LBV}$) is about 1 $M_\odot$, for both the MIX and PRIMORDIAL tracks. Our MESA models reach the proximity of the Eddington limit just at the end of their evolution (~ 1 day before CC); hence, we expect a negligible mass loss from such an opacity-driven process.

Based on these considerations, we now give an estimate of the final BH mass ($M_{\rm BH}$) of the post-collision tracks. Starting from the pre-supernova mass of the star (M_*), we subtract the mass lost because of shocks induced by neutrino emission in a failed supernova (Fernández et al. 2018) as follows:

$$M_{\rm BH} = M_* - \delta M_{\rm G} - M_{\rm ej}, \quad (3)$$

where $\delta M_{\rm G} = 0.3\ M_\odot$ is the instantaneous loss of gravitational mass and $M_{\rm ej}$ is the ejected mass because of neutrino-driven shocks. The last column of Table 2 lists the estimated final BH mass for each track. For this computation, we use the maximum case of $M_{\rm ej}$. For example, in the case of the track POST-SPH, we use $M_{\rm ej} = 0.26\ M_\odot$. This result implies that the final mass of the BH will be about 87 $M_\odot$ (POST-SPH model), lying inside the PI mass gap.

In our study, we did not include the effect of possible chemical asymmetries due to the collision of the two stars, as found by Ballone et al. (2022). Such asymmetries are not followed in our 1d models, but we expect that they do not affect the post-collision evolution. In fact, the PARSEC post-collision tracks, which take into account the energy injected during accretion, become RSGs and develop large convective envelopes. Such convective regions would mix eventual chemical asymmetries in a timescale much faster than the evolutionary timescale of the star (as described in Sect. 3.1). This suggests that eventual chemical asymmetries should be rapidly homogenized in the stellar envelope. In Ballone et al. (2022) the two stars collide head-on, forming a non-rotating post-collision stellar product. In the case of an off-center collision, the post-collision product will be a rotating star. Rotation may lead to a geometrical distortion, to a growth of the stellar core, and to an enhancement of the mass loss. Depending on the amount of angular momentum in the star after the collision and on its evolutionary stage, rotation may change the star's final fate. We will investigate the role of rotation in forthcoming papers.

5 SUMMARY

We have studied the evolution of a post-collision star, by means of detailed stellar evolution calculations with the PARSEC and MESA codes. To reconstruct the post-collision star, we used results from the SPH simulation by Ballone et al. (2022), taking into account the mass lost during the collision (12% of the total mass) and the new chemical profile.

We find that the stellar tracks computed for the post-collision stars avoid PI and evolve until the final CC. Remarkably, the PARSEC and MESA stellar models evolve in a very similar way, ending their life as BSG stars. We estimate the final BH mass by taking into account the possible mass ejected during the final collapse, due to shocks induced by neutrino loss; we find that all of our models lose less than 0.5 $M_\odot$ during the final collapse, because of the relatively high compactness of the stellar envelope ($\xi_{\rm env} = 0.4 - 0.5$).

Thus, we expect that all our models produce BHs with mass ≈ 87 $M_\odot$, within the PI mass gap.

ACKNOWLEDGEMENTS

We thank Morgan MacLeod and Mathieu Renzo for useful discussions. A. Ballone, G. Costa and M. Mapelli acknowledge financial support from the European Research Council for the ERC Consolidator grant DEMOBLACK, under contract no. 770017. This research made use of NumPy (Harris et al. 2020), SciPy (Virtanen et al. 2020), IPython (Perez & Granger 2007). For the plots we used Matplotlib, a Python library for publication quality graphics (Hunter 2007).

DATA AVAILABILITY

The data underlying this article are publicly available at the following link 10.5281/zenodo.6418976.

REFERENCES

Abbott R., et al., 2020a, Phys. Rev. Lett., 125, 101102
Abbott R., et al., 2020b, ApJ, 900, L13
Abbott R., et al., 2021a, arXiv e-prints, p. arXiv:2108.01045
Abbott R., et al., 2021b, arXiv e-prints, p. arXiv:2111.03606
Ballone A., Costa G., Mapelli M., MacLeod M., 2022, arXiv e-prints, p. arXiv:2204.03493
Belczynski K., et al., 2016, A&A, 594, A97
Boekholt T. C. N., Schleicher D. R. G., Fellhauer M., Klessen R. S., Reinoso B., Stutz A. M., Haemmerlé L., 2018, MNRAS, 476, 366
Bressan A. G., Chiosi C., Bertelli G., 1981, A&A, 102, 25
Bressan A., Marigo P., Girardi L., Salasnich B., Dal Cero C., Rubele S., Nanni A., 2012, MNRAS, 427, 127
Brott I., et al., 2011, A&A, 530, A115
Caffau E., Ludwig H. G., Steffen M., Freytag B., Bonifacio P., 2011, Sol. Phys., 268, 255
Chieffi A., et al., 2021, ApJ, 916, 79
Costa G., Girardi L., Bressan A., Marigo P., Rodrigues T. S., Chen Y., Lanza A., Goudfrooij P., 2019a, MNRAS, 485, 4641
Costa G., Girardi L., Bressan A., Chen Y., Goudfrooij P., Marigo P., Rodrigues T. S., Lanza A., 2019b, A&A, 631, A128
Costa G., Bressan A., Mapelli M., Marigo P., Iorio G., Spera M., 2021, MNRAS, 501, 4514
Di Carlo U. N., Giacobbo N., Mapelli M., Pasquato M., Spera M., Wang L., Haardt F., 2019, MNRAS, 487, 2947
Di Carlo U. N., Mapelli M., Bouffanais Y., Giacobbo N., Santoliquido F., Bressan A., Spera M., Haardt F., 2020a, MNRAS, 497, 1043
Di Carlo U. N., et al., 2020b, MNRAS, 498, 495
Di Carlo U. N., et al., 2021, MNRAS, 507, 5132
Farmer R., Fields C. E., Petermann I., Dessart L., Cantiello M., Paxton B., Timmes F. X., 2016, ApJS, 227, 22
Farmer R., Renzo M., de Mink S. E., Marchant P., Justham S., 2019, ApJ, 887, 53
Farmer R., Renzo M., de Mink S. E., Fishbach M., Justham S., 2020, ApJ, 902, L36
Farrell E., Groh J. H., Hirschi R., Murphy L., Kaiser E., Ekström S., Georgy C., Meynet G., 2021, MNRAS, 502, L40
Fernández R., Quataert E., Kashiyama K., Coughlin E. R., 2018, MNRAS, 476, 2366
Ferraro F. R., et al., 2012, Nature, 492, 393

Freitag M., Gürkan M. A., Rasio F. A., 2006, MNRAS, 368, 141
Gaburov E., Lombardi James C. J., Portegies Zwart S., Rasio F. A., 2018, StarSmasher: Smoothed Particle Hydrodynamics code for smashing stars and planets (ascl:1805.010)
Giacobbo N., Mapelli M., Spera M., 2018, MNRAS, 474, 2959
Giersz M., Leigh N., Hypki A., Lützgendorf N., Askar A., 2015, MNRAS, 454, 3150
Glebbeek E., Pols O. R., Hurley J. R., 2008, A&A, 488, 1007
Glebbeek E., Gaburov E., de Mink S. E., Pols O. R., Portegies Zwart S. F., 2009, A&A, 497, 255
Glebbeek E., Gaburov E., Portegies Zwart S., Pols O. R., 2013, MNRAS, 434, 3497
Gürkan M. A., Fregeau J. M., Rasio F. A., 2006, ApJ, 640, L39
Harris C. R., et al., 2020, Nature, 585, 357
Heger A., Woosley S. E., 2002, ApJ, 567, 532
Hunter J. D., 2007, Computing In Science & Engineering, 9, 90
Kippenhahn R., Weigert A., Weiss A., 2012, Stellar Structure and Evolution. Stellar Structure and Evolution: , Astronomy and Astrophysics Library. ISBN 978-3-642-30255-8. Springer-Verlag Berlin Heidelberg, 2012, doi:10.1007/978-3-642-30304-3
Kremer K., et al., 2020, ApJ, 903, 45
Kunitomo M., Guillot T., Takeuchi T., Ida S., 2017, A&A, 599, A49
Ledoux P., 1947, ApJ, 105, 305
Lovegrove E., Woosley S. E., 2013, ApJ, 769, 109
Lovegrove E., Woosley S. E., Zhang W., 2017, ApJ, 845, 103
Maeder A., 1975, A&A, 40, 303
Mapelli M., 2016, MNRAS, 459, 3432
Mapelli M., Sigurdsson S., Colpi M., Ferraro F. R., Possenti A., Rood R. T., Sills A., Beccari G., 2004, ApJ, 605, L29
Mapelli M., Sigurdsson S., Ferraro F. R., Colpi M., Possenti A., Lanzoni B., 2006, MNRAS, 373, 361
Mapelli M., Spera M., Montanari E., Limongi M., Chieffi A., Giacobbo N., Bressan A., Bouffanais Y., 2020, ApJ, 888, 76
Marchant P., Moriya T. J., 2020, A&A, 640, L18
O'Connor E., Ott C. D., 2011, ApJ, 730, 70
Paxton B., Bildsten L., Dotter A., Herwig F., Lesaffre P., Timmes F., 2011, ApJS, 192, 3
Paxton B., et al., 2013, ApJS, 208, 4
Paxton B., et al., 2015, ApJS, 220, 15
Paxton B., et al., 2018, ApJS, 234, 34
Paxton B., et al., 2019, ApJS, 243, 10
Perez F., Granger B. E., 2007, Computing in Science Engineering, 9, 21
Portegies Zwart S., 2019, A&A, 621, L10
Portegies Zwart S. F., McMillan S. L. W., 2002, ApJ, 576, 899
Portegies Zwart S. F., Hut P., McMillan S. L. W., Verbunt F., 1997, A&A, 328, 143
Portegies Zwart S. F., Makino J., McMillan S. L. W., Hut P., 1999, A&A, 348, 117
Portegies Zwart S. F., Baumgardt H., Hut P., Makino J., McMillan S. L. W., 2004, Nature, 428, 724
Powell J., Müller B., Heger A., 2021, MNRAS, 503, 2108
Rahman N., Janka H. T., Stockinger G., Woosley S. E., 2022, MNRAS, 512, 4503
Renzo M., Farmer R., Justham S., Götberg Y., de Mink S. E., Zapartas E., Marchant P., Smith N., 2020a, A&A, 640, A56
Renzo M., Cantiello M., Metzger B. D., Jiang Y. F., 2020b, ApJ, 904, L13
Rizzuto F. P., et al., 2021, MNRAS, 501, 5257
Schwarzschild M., 1958, Structure and evolution of the stars.. Princeton, Princeton University Press, 1958.
Sigurdsson S., Davies M. B., Bolte M., 1994, ApJ, 431, L115
Sills A., Lombardi James C. J., Bailyn C. D., Demarque P., Rasio F. A., Shapiro S. L., 1997, ApJ, 487, 290
Sills A., Faber J. A., Lombardi James C. J., Rasio F. A., Warren A. R., 2001, ApJ, 548, 323
Spera M., Mapelli M., 2017, MNRAS, 470, 4739
Spera M., Mapelli M., Giacobbo N., Trani A. A., Bressan A., Costa G., 2019, MNRAS, 485, 889
Stevenson S., Sampson M., Powell J., Vigna-Gómez A., Neijssel C. J., Szécsi D., Mandel I., 2019, ApJ, 882, 121
Torniamenti S., Rastello S., Mapelli M., Di Carlo U. N., Ballone A., Pasquato M., 2022, arXiv e-prints, p. arXiv:2203.08163
Vigna-Gómez A., Justham S., Mandel I., de Mink S. E., Podsiadlowski P., 2019, ApJ, 876, L29
Vink J. S., Higgins E. R., Sander A. A. C., Sabhahit G. N., 2021, MNRAS, 504, 146
Virtanen P., et al., 2020, Nature Methods, 17, 261
Woosley S. E., 2017, ApJ, 836, 244
Woosley S. E., 2019, ApJ, 878, 49

APPENDIX A: ACCRETION PROCESS HEAT INJECTION

Following Kunitomo et al. (2017) and references therein, we use the parameterization of the heat injected by the accreting material as follows:

$$L_{\rm add} = \frac{\xi_{\rm acc}\, G\, M \dot{M}}{R} \tag{A1}$$

where $\xi_{\rm acc}$ ranges from 0 to 1, and M and R are the mass and radius of the star, respectively. $\dot{M}$ is the accretion rate in $\mathrm{M_\odot yr^{-1}}$. We tested different values for the $\xi_{\rm acc}$ parameter (0.1, 0.5, 1.0). In all cases, we find a similar evolution during the accretion, which causes the star to expand, become a RSG, and reach the same location in the HR diagram. The injected energy is distributed instantaneously inside the star with a simple model, in which the energy is deposited only in an outer layer of the star of mass $m_{\rm ke} = 0.5$ in mass fraction. The energy deposited per unit of mass is:

$$\epsilon_{\rm add} = \left(\frac{L_{\rm add}}{M}\right) \max\left[0, \frac{2}{m_{\rm ke}^2}\left(\frac{M_r}{M} - 1 + m_{\rm ke}\right)\right] \tag{A2}$$

where M_r is the mass coordinate. Finally, we include this additional energy contribution in the structure equation of energy conservation, which reads:

$$\frac{\partial L}{\partial M_r} = \epsilon_{\rm nuc} - \left(T\,\frac{\partial S}{\partial t}\right)_{M_r} + \epsilon_{\rm add}, \tag{A3}$$

where L is the luminosity, T is the temperature, $\epsilon_{\rm nuc}$ is the rate of energy production of nuclear reactions, S is the specific entropy of the shell, and t is the time.

To build the post-collision PARSEC tracks POST-PRIM and POST-SPH, we adopt the following accretion rate prescription:

$$\dot{M}(t) = 10^{-4} \times [(t - T_{\rm start})/dt]^2, \tag{A4}$$

in which $T_{\rm start}$ is the age of the star when the accretion episode begins, t is the stellar age, and dt is the time-step. During accretion, we use a fixed time-step $dt \sim 0.1$ years. To avoid numerical convergence issues, we impose a limit on the maximum accretion rate as follows:

$$\dot{M}(t) = \min\left[\dot{M}(t), 5\ \mathrm{M_\odot/yr}\right] \tag{A5}$$

We stop the accretion when $M_{\rm coll}$ is reached. With the above configuration, the accretion process lasts for about 23 years.

This paper has been typeset from a TEX/LATEX file prepared by the author.